NANO LETTERS

pubs.acs.org/NanoLett Letter

Real-Space Observations of Three-Dimensional Antiskyrmions and Skyrmion Strings

Xiuzhen Yu,* Konstantin V. Iakoubovskii, Fehmi Sami Yasin, Licong Peng, Kiyomi Nakajima, Sebastian Schneider, Kosuke Karube, Takahisa Arima, Yasujiro Taguchi, and Yoshinori Tokura

Cite This: *Nano Lett.* 2022, 22, 9358−9364 Read Online

ACCESS | Metrics & More | Article Recommendations | Supporting Information

ABSTRACT: Nanometric topological spin textures, such as skyrmions (Sks) and antiskyrmions (antiSks), have attracted much attention recently. However, most studies have focused on two-dimensional spin textures in films with inherent or synthetic antisymmetric spin-exchange interaction, termed Dzyaloshinskii−Moriya interaction, although three-dimensional (3D) topological spin textures, such as antiSks composed of alternating Bloch- and Néel-type spin spirals, chiral bobbers carrying emergent magnetic monopoles, and deformed Sk strings, are ubiquitous. To elucidate these textures, we have developed a 3D nanometric magnetic imaging technique, tomographic Lorentz transmission electron microscopy (TEM). The approach enables the visualization of the 3D shape of magnetic objects and their 3D vector field mapping. Here we report 3D vector field maps of deformed Sk-strings and antiSk using the technique. This research approach will lead to discoveries and understanding of fertile 3D magnetic structures in a broad class of magnets, providing insight into 3D topological magnetism.

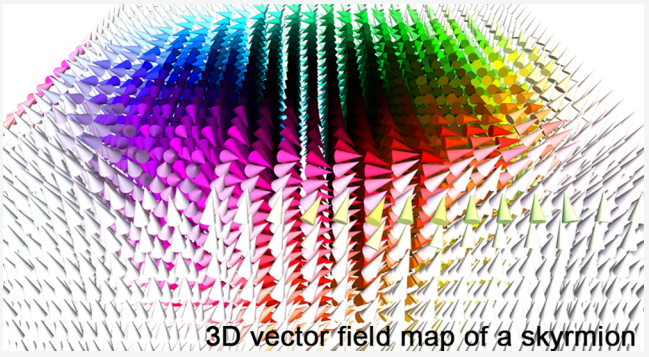

KEYWORDS: *Tomographic Lorentz TEM, 3D vector field mapping, 3D topological spin textures, helimagnet, micromagnetic simulation*

Electron spins and their manipulation have been extensively investigated in various fields of science. In particular, vortex-like spin textures carrying an integer topological charge, such as the skyrmion (Sk) (Figure 1a), have seen intensive research interest because of their emergent electromagnetic properties and information-carrier functionalities.[1−5] The topological charge N of spin textures with magnetic moment distribution $\boldsymbol{m}(\mathbf{r})$ is defined by[1]

$$N = \int \frac{d^2r}{4\pi} \mathbf{n}_r \cdot \left(\frac{\partial \mathbf{n}_r}{\partial x} \times \frac{\partial \mathbf{n}_r}{\partial y} \right) \tag{1}$$

where $\boldsymbol{n}_r = \boldsymbol{m}(\mathbf{r})/|\boldsymbol{m}(\mathbf{r})| = (\cos \varphi(\boldsymbol{r}) \sin \Theta(\boldsymbol{r}), \sin \varphi(\boldsymbol{r}) \cos \Theta(\boldsymbol{r}), \cos \Theta(\boldsymbol{r}))$ is a unit polarization vector, and $\varphi(\boldsymbol{r})$ is described by

$$\varphi(\mathbf{r}) = \Omega\phi + \gamma \tag{2}$$

Here, ϕ is the azimuthal angle of the point $\boldsymbol{r}$, and $\Theta(r)$ is 0 (or π) at $r = 0$ (or ∞), assuming the downward spin at the spin texture's core ($r = 0$) and the upward spin at its periphery ($r \to \infty$). The γ determines the in-plane spin rotation direction (helicity) related to the sign of the Dzyaloshinskii−Moriya interaction (DMI), and Ω is the spin texture's vorticity, +1 for Sks and −1 for antiskyrmions (antiSks),[1] resulting in $N = -1$ for Sk and $N = +1$ for antiSk.

The ideal two-dimensional (2D) topological features of Sk and antiSk, namely the spin-swirling of Bloch-type spiral ($\gamma = \pm\pi/2$) or Néel type spiral ($\gamma = 0$ or π) for a Sk and the alternating Bloch- and Néel-type spirals constituting a circular or square-shaped magnetic domain for antiSks, have been confirmed by theoretical modeling[1,2] and real-space imaging in several magnets[3−7] with inherent broken inversion symmetry and in heterostructured films.[8] However, the features of ideal Sks and antiSks often collapse or deform due to the effects of crystalline imperfections, local intrinsic magnetic anisotropy, and demagnetization on the sample surface in actual materials.[9,10] Such irregular spin textures cannot be well understood through the 2D micrography. Theoretical studies have predicted many intriguing 3D spin textures, such as chiral bobbers[11] and spin-hedgehogs[12] carrying magnetic monopoles, and 3D solitons termed hopfions,[13] for the interpretation of 2D micrography observations.[14−16] However, these 3D topological models have not been directly visualized in chiral-lattice magnets. Recent discoveries of novel transport properties such as giant topological Hall[17,18] and Nernst[19]

Received: August 8, 2022
Revised: October 26, 2022
Published: November 16, 2022

https://doi.org/10.1021/acs.nanolett.2c03142
Nano Lett. 2022, 22, 9358−9364

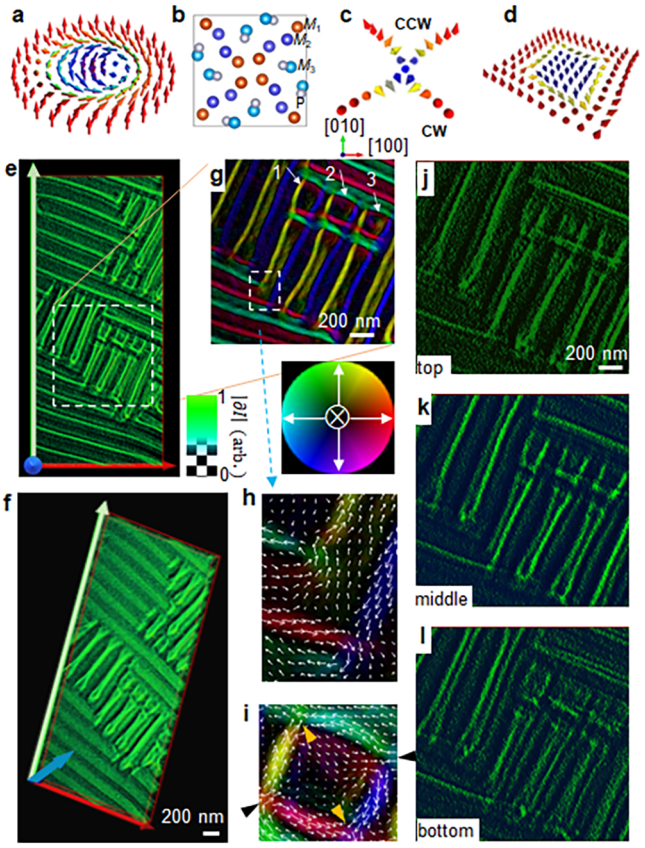

Figure 1. Tomographic Lorentz transmission electron microscopy (TEM) images of antiskyrmions accompanied by orthogonal helices in a noncentrosymmetric magnet $Fe_{1.9}Ni_{0.9}Pd_{0.2}P$ (FNPP) with the M_3P-structure (M: transition metal). (a–d) Schematics of (a) Bloch-type skyrmion, (b) the crystal structure of FNPP viewed from the [001] direction, where the sites M_1, M_2 and M_3 are occupied by Fe, Ni and Pd. (c) Orthogonal helices along the [110] and [1$\bar{1}$0] axes and (d) an antiskyrmion. Color arrows in a-d indicate the direction of electron spins, and CW and CCW stand for clockwise (left-handed) and counterclockwise (right-handed) helicities, respectively. (e,f) Top (e) and oblique views (f) of the 3D magnetic configurations composed of antiskyrmions (square-shape domains) and helices (stripes) in a (001) thin plate of FNPP. The color bar shows the arbitrary intensity. (g) The 2D field map of the area inside the dashed rectangle in panel e. (h,i) Enlarged views of the 2D field map in panel g for (h) orthogonal helices (corresponding to the region surrounded by dashed lines in g) and (i) antiskyrmion #2. The color wheel and white arrows indicate the magnitude and direction of the in-plane fields. Two yellow and two black arrows in panel i indicate Bloch lines in the antiskyrmion. (j–l) Tomographic images of (j) a slice around the top surface, (k) a middle, and (l) around the bottom surface of the magnified 3D magnetic configurations for the surrounding area in panel e. The sample orientations are indicated by the red (x//[110] axis)/green (y//[1$\bar{1}$0] axis)/blue (z//[001] axis) arrows.

effects in chiral-lattice or centrosymmetric magnets hosting nanometric Sks also urge detailed imaging of 3D magnetic configurations. From the perspective of applications, on the other hand, the 3D hybrid topological spin textures with N_{total} = 0 (N = +1 and- 1 for top- and bottom-layer Sks) are proposed in an antiferromagnetic bilayer system[8] and in multilayered films with interfacial DMI.[20] In contrast to a simple Bloch-type or Néel-type spin whirls of Sks, antiSk's texture composed of alternating Bloch- and Néel-type spin spirals is theoretically predicted as a more detailed 3D spin texture. There is also surging interest in deeply understanding 3D nanomagnetism in nanomagnets and related devices.[21] Accordingly, there is a demand to develop a 3D magnetic imaging technique for identifying novel 3D magnetic structures.

Thus far, state-of-the-art 3D magnetic imaging has been performed using X-ray magnetic circular dichroism, which is sensitive to magnetic components parallel to the X-ray beam and allows the collection of 3D resonant elastic X-ray scattering in reciprocal space[22] and maps of the real-space scalar fields in 3D Sk strings in chiral-lattice magnets.[23] Recently, several X-ray studies have focused on 3D magnetic imaging of ferromagnetic magnets at room temperatures (RT), such as Co, permalloy and magnetic heterostructured thin films.[24−26] Among them, the magnetic monopole and 3D magnetization dynamics were observed by X-ray vector nanotomography and time-resolved 3D magnetic imaging in Co nanowires,[24,25] respectively, and the topological charge for 3D magnetic objects was determined by spatially resolved X-ray tomography.[26] Besides X-ray tomography, electron holographic imaging was used for viewing 3D magnetic structures in a heterostructured film,[27] a Co nanowire,[28] and a chiral-lattice magnet FeGe.[29] Mapping the 3D vector field (**B**; hereafter, the field **B** indicates magnetic induction) revealed vortices in the heterostructure and the nanowire and possible Néel-type spin spirals near the sample surface in FeGe. Some studies have also reported 3D reconstruction algorithms and their application to micrometer-scale artificial vortices by tomographic Lorentz TEM[30,31] based on the transport of intensity equation (TIE).[32,33]

This study aims to develop a TEM technique that (1) can directly visualize complex 3D spin textures like Sks and antiSks exhibiting Bloch lines, (2) has a spatial resolution high enough to view magnetic monopole involved in the broken Sk strings, and (3) should be much easier to perform than the holography technique. We chose tomographic Lorentz TEM and built an algorithm for 3D vector field reconstruction allowing real-space observation of 3D topological spin textures, such as antiSks, Sk strings, and the magnetic monopole. The requirement for the high spatial resolution is satisfied with Lorentz TEM, which has a spatial resolution approaching 2 nm[10] (5 nm in the present study). However, in contrast with the conventional tomographic TEM which is performed in the in-focus mode, tomographic Lorentz TEM requires defocusing the image. Defocusing brings up the dark/bright contrast corresponding to spin textures like Sk and antiSk, which vanishes in focus (see details in the section "Tomographic Lorentz TEM" in Supporting Information (SI)). 3D reconstruction of the tilt series of 2D images obtained in the defocus mode is not straightforward. To overcome critical challenges, such as stabilizing antiSk and Sk strings at zero magnetic field in TEM samples, image blurring, overlap of the neighboring spin textures and reducing diffraction contrasts arising from crystalline orientations and defects with changing the tilt angle, we optimized the sample geometry and defocus conditions, and reduced the surface roughness of the samples.

First, to reveal the 3D spin textures of antiSks, we have examined the magnetic configurations of single-crystal $Fe_{1.9}Ni_{0.9}Pd_{0.2}P$ (FNPP) at zero magnetic field and RT by the tomographic Lorentz TEM. FNPP has a tetragonal structure with S_4 symmetry (Figure 1b).[7] The broken inversion symmetry of the crystal structure gives rise to DMI. The $I\bar{4}$ space group provides two orthogonal spin-spiral wavevectors

https://doi.org/10.1021/acs.nanolett.2c03142
Nano Lett. 2022, 22, 9358−9364

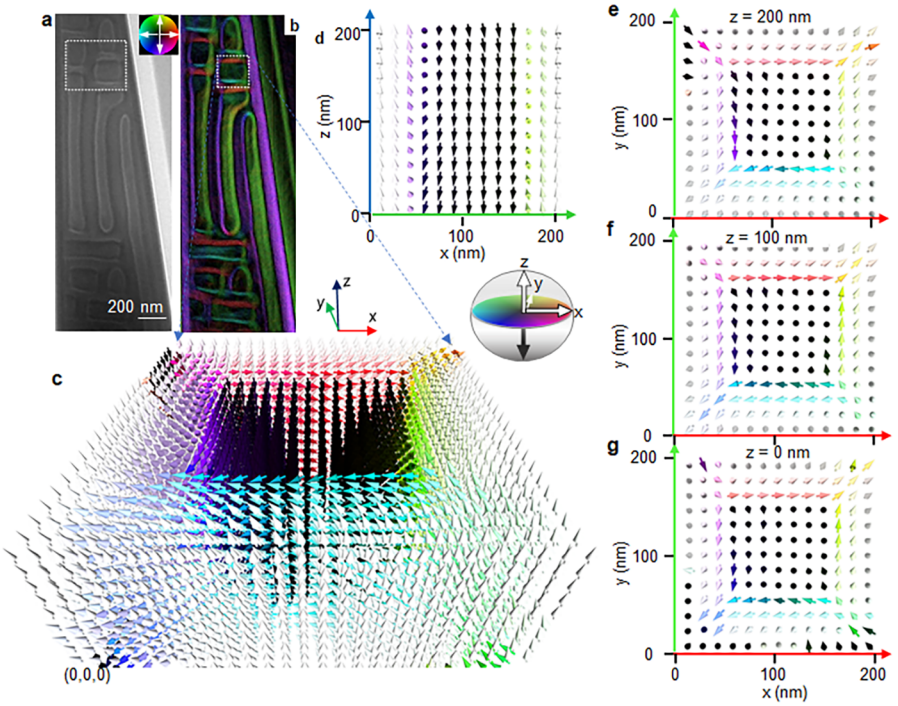

Figure 2. Three-dimensional (3D) field maps of an antiskyrmion observed in a needle-like FNPP. (a) Under-focus Lorentz TEM image and (b) its magnetic induction field map. The color wheel shows the in-plane-field direction at every point. (c) 3D vector field map of an antiskyrmion, corresponding to the area surrounded by white dashed lines in panel b. The direction of the colored arrows is indicated by a color ball (the upper-right corner of panel c). (d) Field maps of the antiskyrmion in the xz plane at y = 100 nm. Dark arrows show magnetic fields pointing down ($-z$ direction) at the antiskyrmion core, while bright arrows indicate the fields pointing up at the periphery of the antiskyrmion. (e–g) Field maps of the antiskyrmion in the xy plane at (e) z = 200 nm (top-surface slice), (f) z = 100 nm (central slice), and (g) z = 0 nm (bottom-surface slice).

with opposite spin helicities, right-handed (CCW) and left-handed (CW) screws, along the [110] and [1$\bar{1}$0] axes (Figure 1c), respectively. The competition among the ferromagnetic exchange interaction, dipolar interaction, and DMI enables the formation of antiSks (Figure 1d) above RT when an external magnetic field is applied along the [001] axis. We adopted field cooling (FC, see details in SI) to stabilize a mixture of helices (stripes in Figures 1e,f) with wavevectors parallel to the [110] and [1$\bar{1}$0] axes and antiSks (square-shape textures in Figure 1e) at zero field in a (001) FNPP thin plate with a dimension of 1.53 × 3.36 × 0.2 $(\mu m)^3$. Before investigating the 3D magnetic configurations in FNPP, we identified antiSks and orthogonal helices. We analyzed a series of 2D defocus Lorentz TEM images (Figure S1a,b in SI) for the surrounding region in Figure 1e to obtain their 2D phase (Figure S1c) and hence corresponding magnetic induction maps (Figure 1g) by performing TIE[32,33] analyses (see details in SI).The magnified 2D field maps for the helices (Figure 1h) and antiSk#2 (Figure 1i) clearly demonstrate the perpendicular nature of helices with CW (blue and yellow stripes) and CCW (red and green stripes) and an antiSk composed of four alternatingly arranged Bloch lines with Néel-type spirals and Bloch-type spirals.[34]

We developed a tomographic Lorentz TEM technique to reveal the 3D spin texture in the antiSk and identify its topological nature. First, a tilt series of 2D projected Lorentz TEM images around the x and y axes was recorded for tilt angles ranging from −50° to +50° at 2° intervals using the script package "Recorder" (see details in Methods and Figure S2 in SI). Figure S3 presents the dual-axis (x and y) tilt series of projected 2D Lorentz TEM images and zero-tilt induction field map for a single antiSk. The changes of projected Lorentz TEM images of the antiSk with the tilt angle qualitatively agree with the simulations (Figure S4). Then, we construct the 3D magnetic configurations from the tilt series of the 2D Lorentz TEM images using the TEM tomography package "Composer" followed by a 3D viewer "Visualizer". Figure 1e,f show top and oblique views extracted from the 3D shape of magnetic configurations (see Movie S1 in SI), respectively, which are represented by the difference of intensities $|I(xyz + \Delta f) - I(xyz - \Delta f)|$ (Δf = 100 μm) between overfocused and underfocused Lorentz TEM images related to the phase differential $\nabla^2\varphi(xyz)$ of the electron wave. The twisted textures appear green, whereas the linear spin textures show a darker color. Notably, the tomographic Lorentz TEM results (Figure 1f) clearly reveal that the magnetic twists align almost uniformly through the thickness of the sample. Although spin texture does not significantly change along the z-axis, intensity difference appears between the surfaces and center, as shown in Figure 1j–l: the intensity is weaker around the top/bottom surface (Figures 1j–l). Meanwhile it becomes stronger deep in bulk (Figure 1k), suggesting a hybridized magnetic structure of Bloch-type twists in bulk and Néel-type twists at the surfaces, which should decrease the intensity of magnetic signals due to the cancellation of the in-plane magnetic moments projected in Lorentz TEM images. On the other hand, the demagnetization field also affects the surface spin textures, which are represented by simulated 3D spin textures for an antiSk (see details in Figure S5): 1) expansion of the domain walls on the top and bottom surfaces; 2) a diagonal deformation on the top and bottom surfaces; 3) a decrease in out-of-plane magnetic induction at the surfaces. Compared to the structure in the central slice (Figure 1k), the expansion and deformation of spin textures, as well as the decrease of the intensity on the top and bottom surfaces, appear in the intensity reconstructions in

https://doi.org/10.1021/acs.nanolett.2c03142
Nano Lett. 2022, 22, 9358−9364

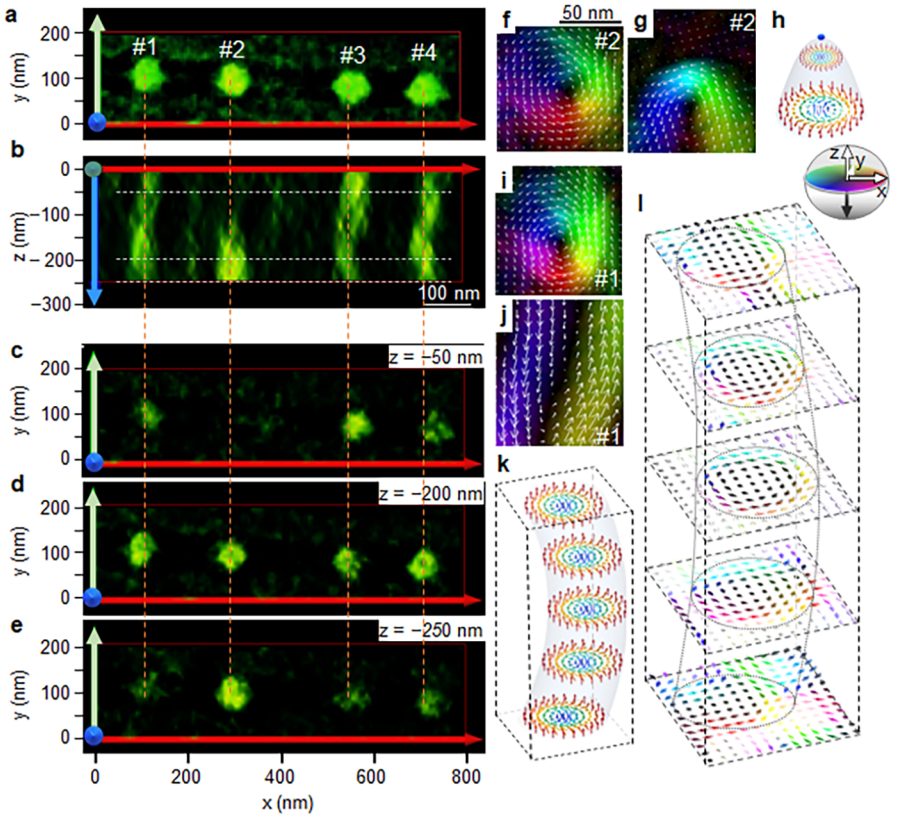

Figure 3. Tomographic Lorentz TEM images (a-e) and vector field maps (f-g, i-l) of a chiral bobber and deformed skyrmion strings in the chiral-lattice micromagnet $Co_9Zn_9Mn_2$ with dimensions of $1 \times 0.2 \times 0.25$ $(\mu m)^3$. (a) Top and (b) cross-section views of three isolated skyrmion strings (numbered #1, #3 and #4 in panel a) and one chiral bobber (#2 in panel a) observed by tomographic Lorentz TEM. (c−e) Slices of the 3D magnetic configurations of skyrmion strings and the bobber at different thicknesses marked by white dashed lines in panel b: (c) near the top-surface ($z = -50$ nm), (d) close to the sample center ($z = -200$ nm), and (e) near the bottom-surface ($z = -250$ nm). Orange dashed lines are eye guides for strings. The colored arrows in panels a−e indicate the x (red), y (green) and z (blue) axes. (f−g,i,j) 2D projections of field maps at tilt angles of (f,i) 0° and (g,j) 50° for (f,g) the bobber #2, and (i-j) a skyrmion string #1. (h,k) Schematics of (h) the chiral bobber carrying a magnetic monopole (a blue dot at the end), (k) a deformed skyrmion string. (l) Several XY-slices of a 3D vector field map of deformed skyrmion string #4 from top to bottom. The colored arrows encoded by the color ball show the magnetic field swirling while dark and white arrows indicate the down and up field directions, respectively.

Figure 1j and Figure 1l, respectively, in agreement with the simulations. While we have experimentally identified the antiSk's bulk 3D structure here, higher tilt angle micrographs are needed to reveal the surface structure.

To reconstruct 3D vector field maps of the antiSks from series of 2D field maps obtained by sequentially tilting the sample around the x and y axes, we prepared a needle-like sample, as shown in Figure 2a. The 2D Lorentz TEM image (a, underfocused) and corresponding magnetic induction field map (b) show a mixture of antiSks and in-plane helices at zero magnetic field and RT. We recorded a tilt series of underfocused and overfocused Lorentz TEM images, with tilt angles α and β around the y and x axes, respectively, ranging from −50° to +50° with a 2° increment. We then extracted the corresponding phase images (Figure S6) and magnetic induction field at every tilt angle from −35° to +35° by performing TIE analyses; note here that the intensity of the magnetic structure became extremely weak due to the loss of electron wave amplitude at the high tilt angles. The 3D field maps were obtained using the software "TomoPy" (see details in Figure S2 and the related description of the 3D reconstruction procedures in SI). Figure S7 shows the 3D vector-field maps (a), the corresponding (b) XY map at z = 100 nm of the surrounding area in Figure 2a composed of two antiSks and two elongated spin textures, and (c) 3D vector field map obtained by reconstructing a tilt series of simulated images for an ideal antiSk with a tilt angle range of ±35°, respectively. Figure S7a reveals complicated spin textures including twisted textures in the antiSk (the area surrounded with a dashed rectangle in Figure S7b). To show the vector field map of the antiSk clearer, we plot the 3D fields for one antiSk (surrounded by white dashed lines in Figure 2b) in Figure 2c,d, representing the downward moments in the core, as indicated by dark arrows, and the upward moments at the periphery, as indicated by bright arrows. The twisted moments (gradational purple and green arrows in Figures 2c,d) between the downward (the z-direction) and upward (the +z direction) moments, and four Bloch lines (Néel-type spirals) are discerned at the four corners (Figure 2c,e−g), are discerned. Between the neighboring Bloch lines, the gradational red arrows display the magnetic moments pointing to the right ($+x$ direction), the blue arrows show the magnetic moments pointing to the left ($-x$ direction), and the green and purple arrows indicate the magnetic moments pointing to the + y and the- y directions, respectively. The field distributions at the top (e, z = 200 nm) and bottom (g, z = 0 nm) surfaces are almost the same as those at the center (g) (z = 100 nm), except for that at the corners of field maps (possibly induced by the

https://doi.org/10.1021/acs.nanolett.2c03142
Nano Lett. 2022, 22, 9358−9364

neighboring spin textures in the sample), indicating a simple antiSk configuration. The good agreement between experiment (Figure 2c) and simulation (Figure S7c) validates our tomographic Lorentz TEM observations and vector field reconstructions. However, the relatively small range of experimentally accessible tilt angles (known as the "missing-wedge" problem) should reduce the accuracy of 3D reconstruction for all tomography techniques. (The main reasons for the limitation of the tilt angle were 1) the isolated zero-field antiSks can not be stabilized in samples thinner than 130 nm. Hence thicker samples were used but their imaging at 200 kV-Lorentz TEM would become difficult at large tilt angle; 2) the mixture of antiSks and helices is hard to disentangle at high tilt angle.) Note that the difference between the vector field and the magnetization maps of an ideal antiSk was observed by micromagnetic simulations (Figure S8a,b) and Lorentz TEM observations (Figure S8c). The difference originates from stray fields around Bloch lines, where the divergence of magnetization, and hence magnetic charge should not be zero. However, such stray fields hardly affect the fundamental 3D topological features of the antiSk identified here (Figure 2).

We apply the tomographic Lorentz TEM to examine topological defects, such as monopoles involved in broken Sk strings.[9,10,12,15] One such example, the chiral bobber[11] (Figure 3h) carrying a magnetic monopole at its end, attracts much attention as the most typical 3D topological defect, yet it has not been confirmed by 3D real-space imaging. Here, we used FC process to form metastable zero-field Sks in a chiral-lattice ($P4_132$ space group) magnet $Co_9Zn_9Mn_2$[35,36] with a size of 1 × 0.2 × 0.25 $(\mu m)^3$. We confirmed the isolated 3D string-like structures by tomographic Lorentz TEM (Movie S2 in SI), as shown by an XY top view (Figure 3a) and an XZ cross-section at y = 100 nm (Figure 3b). The circular domains with an average diameter of about 80 nm are projected in the XY plane. The Sks #1−4 are discerned as curved strings (see a schematic of the deformed Sk string in Figure 3k) in the XZ cross-section image. In particular, a short one (#2) ends near the center of the magnet (z = −150 nm), exhibiting a chiral bobber-like feature (Figure 3h). Such chiral bobber-like structures and deformed strings are also confirmed by several XY-slices taken at different z-values (Figure 3c−e). The slice at z = −50 nm close to the top surface exhibits only three circular domains corresponding to strings #1, #3, and #4, whereas chiral bobber #2 is absent. Meanwhile, the slice at z = −200 nm close to the bottom surface displays all circular domains with comparable intensities, and the slice at z = −250 nm at the bottom surface reveals the strongest intensity for chiral bobber #2, but extremely weak intensities for Sk strings #1, #3, and #4. These observations directly demonstrate the 3D aspects of deformed Sk strings #1, #3, and #4 and chiral bobber #2 close to the bottom surface.

To confirm the deformed Sk string and chiral bobber, we analyzed Lorentz TEM images of the top and oblique views of the string and bobber by the TIE. The induction field maps at zero tilt (Figure 3f,i) and the projected field maps at 50° tilt for the bobber (Figure 3g) and deformed string #1 (Figure 3j) show that there is no significant difference for these spin textures as viewed along the normal to the sample plate (zero tilt). However, the oblique field maps discern topological distinctions between the string and the bobber (Figures 3g,j): the string extends to the top surface, whereas the bobber ends deep within bulk, revealing monopole textures at the bobber's end.

To identify the spin textures of the deformed string in bulk, we reconstructed the 3D vector field map of Sk string #4. Figure S9 shows a series of phase images of the Sk string obtained by sequentially tilting the sample around both the x- and y- axes in a 5°-step increment. We used this series of phase images to calculate B_x, B_y, and B_z and then reconstructed the 3D vector field map for the Sk string. The field map slices through the length of the Sk string (Figure 3l), demonstrate that the spin swirls remain in the interior while collapsing at both the top and bottom surfaces (see changes in colored arrows). Figure 3l also reveals that the string is highly deformed deep within bulk while maintaining its vorticity and helicity throughout the string length (Figure S10). Our tomographic Lorentz TEM results provide the first experimental evidence of the 3D topological spin textures associated with highly deformed metastable Sk strings in a chiral-lattice magnet at zero magnetic field and RT.

From the application viewpoint, the 3D Lorentz TEM tomography is a relatively simple technique that can be realized with a standard commercial transmission electron microscope in its basic configuration. Data processing is relatively quick and can be performed during the imaging process. The 3D tomographic Lorentz TEM imaging technique developed here will enable the visualization and magnetic vector mapping of unknown nanometric 3D magnetic configurations with nontrivial topology in magnetic materials.

■ ASSOCIATED CONTENT

Supporting Information

The Supporting Information is available free of charge at https://pubs.acs.org/doi/10.1021/acs.nanolett.2c03142.

Materials preparation, methods and additional data used to support the conclusion in the present paper; Figures S1−S10 (PDF)

Data for zero-field antiSks, Sk-strings and their tilt series of Lorentz TEM images, the corresponding simulated images, and their 3D vector field maps and corresponding simulated 3D field maps, and tomographic Lorentz TEM for antiskyrmions (MP4)

For skyrmion strings (MP4)

■ AUTHOR INFORMATION

Corresponding Author

Xiuzhen Yu − *RIKEN Center for Emergent Matter Science (CEMS), Wako 351-0198, Japan*; orcid.org/0000-0003-3136-7289; Email: yu_x@riken.jp

Authors

Konstantin V. Iakoubovskii − *RIKEN Center for Emergent Matter Science (CEMS), Wako 351-0198, Japan*

Fehmi Sami Yasin − *RIKEN Center for Emergent Matter Science (CEMS), Wako 351-0198, Japan*; orcid.org/0000-0001-9382-7565

Licong Peng − *RIKEN Center for Emergent Matter Science (CEMS), Wako 351-0198, Japan*

Kiyomi Nakajima − *RIKEN Center for Emergent Matter Science (CEMS), Wako 351-0198, Japan*

Sebastian Schneider − *RIKEN Center for Emergent Matter Science (CEMS), Wako 351-0198, Japan*

https://doi.org/10.1021/acs.nanolett.2c03142
Nano Lett. 2022, 22, 9358−9364

Kosuke Karube − *RIKEN Center for Emergent Matter Science (CEMS), Wako 351-0198, Japan*
Takahisa Arima − *RIKEN Center for Emergent Matter Science (CEMS), Wako 351-0198, Japan; Department of Advanced Materials Science, University of Tokyo, Kashiwa 277-8561, Japan*
Yasujiro Taguchi − *RIKEN Center for Emergent Matter Science (CEMS), Wako 351-0198, Japan*
Yoshinori Tokura − *RIKEN Center for Emergent Matter Science (CEMS), Wako 351-0198, Japan; Department of Applied Physics and Tokyo College, University of Tokyo, Tokyo 113-8656, Japan;* orcid.org/0000-0002-2732-4983

Complete contact information is available at: https://pubs.acs.org/10.1021/acs.nanolett.2c03142

Author Contributions

X.Y., Y. Taguchi, T.A. and Y.Tokura conceived the project. X.Y. performed tomographic Lorentz TEM, analyzed the experimental data, and wrote the manuscript with Y. Tokura. K.V.I. developed the algorithm for the 3D vector field map reconstruction and wrote the related description in the SI. F.S.Y. contributed to the antiskyrmion simulations and wrote the corresponding description in the SI. L.C.P. and K.N. prepared TEM samples. K.K. and Y. Taguchi synthesized the bulk single-crystal samples. All authors discussed the data and commented on the manuscript.

Notes

The authors declare no competing financial interest.

■ ACKNOWLEDGMENTS

The authors would like to thank Jan Masell, Toshiaki Tanigaki, Yoshio Takahashi, Max Hirschberger, Wataru Koshibae, Naoto Nagaosa, and Sadamichi Maekawa for fruitful discussions and Mari Ishida for technical support. This work was supported in part by Grants-In-Aid for Scientific Research (A) (Grant 19H00660) and Grant-in-Aid for Early-Career Scientists (Grant 20K15164) from the Japan Society for the Promotion of Science (JSPS) and the Japan Science and Technology Agency (JST) CREST program (Grant JPMJCR20T1), Japan.

■ REFERENCES

(1) Nagaosa, N.; Tokura, Y. Topological properties and dynamics of magnetic skyrmions. *Nat. Nanotechnol.* **2013**, *8*, 899−911.
(2) Bogdanov, A. N.; Panagopoulos, C. Physical foundations and basic properties of magnetic skyrmions. *Nat. Rev. Phys.* **2020**, *2*, 492−498.
(3) Mühlbauer, S.; et al. Skyrmion Lattice in a Chiral Magnet. *Science* **2009**, *323*, 915−919.
(4) Yu, X. Z.; et al. Real-space observation of a two-dimensional skyrmion crystal. *Nature* **2010**, *465*, 901−904.
(5) Tokura, Y.; Kanazawa, N. Magnetic skyrmion materials. *Chem. Rev.* **2021**, *121*, 2857−2897.
(6) Nayak, A. K.; et al. Magnetic antiskyrmions above room temperature in tetragonal Heusler materials. *Nature* **2017**, *548*, 561−566.
(7) Karube, K.; et al. Room-temperature antiskyrmions and sawtooth surface textures in a non-centrosymmetric magnet with S_4 symmetry. *Nat. Mater.* **2021**, *20*, 335−340.
(8) Legrand, W.; et al. Room-temperature stabilisation of antiferromagnetic skyrmions in synthetic antiferromagnets. *Nat. Mater.* **2020**, *19*, 34−42.
(9) Kagawa, F.; et al. Current-induced viscoelastic topological unwinding of metastable skyrmion strings. *Nat. Commun.* **2017**, *8*, 1332.
(10) Yu, X. Z.; et al. Real-space observation of topological defects in extended skyrmion strings. *Nano Lett.* **2020**, *20*, 7313−7320.
(11) Rybakov, F. N.; Borisov, A. B.; Blügel, S.; Kiselev, N. S. New type of particle-like state in chiral magnets. *Phys. Rev. Lett.* **2015**, *115*, 117201.
(12) Milde, P.; et al. Unwinding a skyrmion lattice by magnetic monopoles. *Science* **2013**, *340*, 1076−1080.
(13) Tai, J. B.; Smalyukh, I. I. Three-dimensional crystals of adaptive knots. *Science* **2019**, *365*, 1449−1453.
(14) Zheng, F.; et al. Experimental observation of chiral magnetic bobbers in B20-type FeGe. *Nat. Nanotechnol.* **2018**, *13*, 451−455.
(15) Birch, M. T.; et al. Real-space imaging of confined magnetic skyrmion tubes. *Nat. Commun.* **2020**, *11*, 1726.
(16) Kent, N.; et al. Creation and observation of Hopfions in magnetic multilayer systems. *Nat. Commun.* **2021**, *12*, 1562.
(17) Neubauer, A.; et al. Topological Hall effect in phase A of MnSi. *Phys. Rev. Lett.* **2009**, *102*, 186602.
(18) Kurumaji, T.; et al. Skyrmion lattice with a giant topological Hall effect in a frustrated triangular-lattice magnet. *Science* **2019**, *365*, 914−918.
(19) Hirschberger, M.; et al. Topological Nernst effect of two-dimensional skyrmion lattice. *Phys. Rev. Lett.* **2020**, *125*, 076602.
(20) Legrand, W.; et al. Hybrid chiral domain walls and skyrmions in magnetic multilayers. *Sci. Adv.* **2018**, *4*, eaat0415.
(21) Burks, E. C.; et al. 3D Nanomagnetism in low density interconnected nanowire networks. *Nano Lett.* **2021**, *21*, 716−722. Fang, M.; et al. Non-planar geometrical effects on the magneto-electrical signal in a three-dimensional nanomagnetic circuit. *ACS Nano* **2021**, *15*, 6765−6773.
(22) Zhang, S.; et al. Reciprocal space tomography of 3D skyrmion lattice order in a chiral magnet. *Proc. Natl. Acad. Sci. U. S. A.* **2018**, *115*, 6386−639.
(23) Seki, S.; et al. Direct visualisation of three-dimensional shape of skyrmion strings in a noncentrosymmetric magnet. *Nat. Mater.* **2022**, *21*, 181−187.
(24) Donnelly, C.; et al. Three-dimensional magnetization structures revealed by X-ray vector nanotomography. *Nature* **2017**, *547*, 328−331.
(25) Donnelly, C.; et al. Time-resolved imaging of three-dimensional nanoscale magnetization dynamics. *Nat. Nanotechnol.* **2020**, *15*, 356−360.
(26) Hierro-Rodriguez, A.; et al. Revealing 3D magnetization of thin films with soft X-ray tomography: magnetic singularities and topological charges. *Nat. Commun.* **2020**, *11*, 6382.
(27) Tanigaki, T.; et al. Three-dimensional observation of magnetic vortex cores in stacked ferromagnetic discs. *Nano Lett.* **2015**, *15*, 1309−1314.
(28) Wolf, D.; et al. 3D magnetic induction maps of nanoscale materials revealed by electron holographic tomography. *Chem. Mater.* **2015**, *27*, 6771−6778.
(29) Wolf, D.; et al. Unveiling the three-dimensional spin texture of skyrmion tubes. *Nat. Nanotechnol.* **2022**, *17*, 250−255.
(30) Llandro, J.; et al. Visualising the magnetic structure in 3D nanoscale Ni-Fe gyroid networks. *Nano Lett.* **2020**, *20*, 3642−3650.
(31) Phatak, C.; Petford-Long, A. K.; De Graef, M. Three-dimensional study of the vector potential of magnetic structures. *Phys. Rev. Lett.* **2010**, *104*, 253901.
(32) Ishizuka, K.; Allman, B. Phase measurement of atomic resolution image using transport of intensity equation. *J. Electron Microsc.* **2005**, *54*, 191−197.
(33) McVitie, S.; Cushley, M. Quantitative Fresnel Lorentz microscopy and the transport of intensity equation. *Ultramicroscopy* **2006**, *106*, 423−431.
(34) Peng, L. C.; et al. Controlled transformation of skyrmions and antiskyrmions in a non-centrosymmetric magnet. *Nat. Nanotechnol.* **2020**, *15*, 181−186.

(35) Tokunaga, Y.; et al. A new class of chiral materials hosting magnetic skyrmions beyond room temperature. *Nat. Commun.* **2015**, *6*, 7638.
(36) Karube, K.; et al. Skyrmion formation in a bulk chiral magnet at zero magnetic field and above room temperature. *Phys. Rev. Mater.* **2017**, *1*, 074405.

https://doi.org/10.1021/acs.nanolett.2c03142
Nano Lett. 2022, 22, 9358−9364